Aalto University

OPEN ACCESS

This is an electronic reprint of the original article.
This reprint may differ from the original in pagination and typographic detail.

Sintonen, Sakari; Rudzinski, Mariusz; Suihkonen, Sami; Jussila, Henri; Knetzger, Michael; Meissner, Elke; Danilewsky, Andreas; Tuomi, Turkka O.; Lipsanen, Harri

Synchrotron radiation x-ray topography and defect selective etching analysis of threading dislocations in GaN.

Published in:
Journal of Applied Physics

DOI:
10.1063/1.4893901

Published: 01/01/2014

Document Version
Publisher's PDF, also known as Version of record

Please cite the original version:
Sintonen, S., Rudzinski, M., Suihkonen, S., Jussila, H., Knetzger, M., Meissner, E., Danilewsky, A., Tuomi, T. O., & Lipsanen, H. (2014). Synchrotron radiation x-ray topography and defect selective etching analysis of threading dislocations in GaN. *Journal of Applied Physics*, *116*(8), 1-9. Article 083504. https://doi.org/10.1063/1.4893901

This material is protected by copyright and other intellectual property rights, and duplication or sale of all or part of any of the repository collections is not permitted, except that material may be duplicated by you for your research use or educational purposes in electronic or print form. You must obtain permission for any other use. Electronic or print copies may not be offered, whether for sale or otherwise to anyone who is not an authorised user.

Synchrotron radiation x-ray topography and defect selective etching analysis of threading dislocations in GaN

Sakari Sintonen, Mariusz Rudziński, Sami Suihkonen, Henri Jussila, Michael Knetzger, Elke Meissner, Andreas Danilewsky, Turkka O. Tuomi, and Harri Lipsanen

Citation: Journal of Applied Physics **116**, 083504 (2014); doi: 10.1063/1.4893901

View online: http://dx.doi.org/10.1063/1.4893901

View Table of Contents: http://aip.scitation.org/toc/jap/116/8

Published by the American Institute of Physics

AIP | Journal of Applied Physics

Save your money for your research.
It's now FREE to publish with us -
no page, color or publication charges apply.

Publish your research in the
Journal of Applied Physics
to claim your place in applied
physics history.

CrossMark click for updates

Synchrotron radiation x-ray topography and defect selective etching analysis of threading dislocations in GaN

Sakari Sintonen,[1,a)] Mariusz Rudziński,[2] Sami Suihkonen,[1] Henri Jussila,[1] Michael Knetzger,[3] Elke Meissner,[3] Andreas Danilewsky,[4] Turkka O. Tuomi,[1] and Harri Lipsanen[1]

[1]*Department of Micro- and Nanosciences, Aalto University School of Electrical Engineering, 02150 Espoo, Finland*
[2]*Epitaxy Department, Institute of Electronic Materials Technology, 01-919 Warsaw, Poland*
[3]*Fraunhofer Institute for Integrated Systems and Device Technology, 91058 Erlangen, Germany*
[4]*Kristallographie Institut für Geo- und Umweltnaturwissenschaften, Albert-Ludwigs-Universität Freiburg, 79104 Freiburg, Germany*

(Received 9 June 2014; accepted 13 August 2014; published online 25 August 2014)

The crystal quality of bulk GaN crystals is continuously improving due to advances in GaN growth techniques. Defect characterization of the GaN substrates by conventional methods is impeded by the very low dislocation density and a large scale defect analysis method is needed. White beam synchrotron radiation x-ray topography (SR-XRT) is a rapid and non-destructive technique for dislocation analysis on a large scale. In this study, the defect structure of an ammonothermal c-plane GaN substrate was recorded using SR-XRT and the image contrast caused by the dislocation induced microstrain was simulated. The simulations and experimental observations agree excellently and the SR-XRT image contrasts of mixed and screw dislocations were determined. Apart from a few exceptions, defect selective etching measurements were shown to correspond one to one with the SR-XRT results. © *2014 AIP Publishing LLC*. [http://dx.doi.org/10.1063/1.4893901]

I. INTRODUCTION

GaN based optoelectronic and power devices have raised the demand of low defect density native GaN substrates. Consequently, various methods such as hydride vapour phase epitaxy, high pressure nitrogen solution growth, and ammonothermal growth have been employed to achieve high crystal quality GaN.[1] The ammonothermal growth is considered an efficient and scalable bulk GaN growth method, and high quality ammonothermal crystals have been achieved by several groups.[2–5] To sustain the continuous improvement of bulk GaN crystal quality, it is imperative to characterize the defect structure. However, due to the low defect density (as low as $5 \times 10^3\,\mathrm{cm}^{-2}$) in state of the art crystals,[6] defect characterization with conventional methods suitable for higher dislocation density materials is becoming increasingly difficult.

White beam synchrotron radiation x-ray topography (SR-XRT) is a convenient and non-destructive characterization method suited for materials with dislocation density $\sim 10^4\,\mathrm{cm}^{-2}$ and below.[7] Synchrotron radiation provides an intense beam with very low divergence, enabling rapid imaging of dislocations over large areas. In SR-XRT, the beam is diffracted by the sample and the diffracted x-rays are recorded onto an x-ray film. The diffraction spot, often referred to as the topograph, provides information on the microstrain in form of diffraction contrast variation. SR-XRT is extremely sensitive to microstrain and as any dislocation will induce microstrain, the dislocation is seen as contrast variation in the topograph. In white beam SR-XRT, several diffraction spots are recorded simultaneously without the need of tedious sample alignment, since the continuous wavelength distribution ensures diffraction conditions are met for a multitude of lattice planes. For reviews on SR-XRT, see Refs. 8–10.

SR-XRT has been used scarcely in GaN characterization mostly because of the relatively high dislocation density in earlier GaN crystals. The method has however been used to identify grain boundaries in hydride vapour phase epitaxy grown GaN boules[11] and ammonothermal GaN needles[12] as well as grain boundaries, cracks, and micropores in GaN grown on SiC substrates.[13] A more detailed topography study using a laboratory x-ray source identified grain boundaries and dislocations in GaN crystals grown by the high-pressure/high-temperature method.[14] Ammonothermal GaN has also been characterized by positron annihilation spectroscopy[15] x-ray diffraction and micro-Raman measurements.[16] Our recent SR-XRT study on ammonothermal GaN reported on defects with similar appearance to micropipes in SiC[17] and raised the question if the observed defects are also super screw dislocations or micropipes.

This study discusses the back reflection SR-XRT image contrast of threading screw dislocations (TSD) and threading mixed dislocations (TMD) in c-plane GaN. Two distinct SR-XRT contrast types were determined corresponding to screw and mixed type dislocations. The TSD image consists of a symmetric white circular area with a dark circumference, whereas the TMD image has asymmetric black to white contrast with six different contrast directions. Screw dislocation contrast in symmetric 0008 back reflection SR-XRT was simulated using a geometrical approach adopted from previously reported successful SiC micropipe and super screw dislocation characterization.[18,19] Simulations

a)sakari.sintonen@aalto.fi

 © 2014 AIP Publishing LLC

of screw dislocations agree excellently with experimental images of dislocations in ammonothermal GaN. Defect selective etching (DSE) measurements support the SR-XRT results. The existence of nanopipes, micropipes, and super screw dislocations in GaN has been a subject of debate and comparison of SR-XRT, and DSE results show that these hitherto unknown defects are not micropipes, but a collection of closely spaced threading screw dislocations. SR-XRT and DSE results suggest further that the threading edge dislocation (TED) density in the ammonothermal GaN sample is negligibly low.

II. EXPERIMENTAL

The studied sample was a 350 μm thick free-standing c-plane GaN wafer grown by the ammonothermal method,[2] provided by Ammono S.A. The front side of the GaN wafer was polished ready for epitaxy by chemo-mechanical polishing to $\leq$0.5 nm root mean square roughness. This is of great importance since scratches and sub-surface damage very effectively obscure the defect structure image in SR-XRT. Back reflection topographs were recorded at the white beam TopoTomo beamline[20] synchrotron source ANKA at Karlsruhe Institute of Technology with particle energy 2.5 GeV on high resolution Slavich holographic films. The critical energy of the ANKA storage ring is $\epsilon_c = 6.2$ keV and the photon flux at ϵ_c is $\Phi = 8 \times 10^{12}$ photons/s/0.1%BW/mrad. The image resolution is greatly enhanced by the soft x-radiation via the absence of higher energy wavelength harmonics. The typical back reflection exposure time was 30 s with electron current 200 mA. Images were recorded with the sample tilted 7.5° about the horizontal axis perpendicular to the incident beam and sample to film distance 80 mm. Symmetric 0008 and asymmetric $02\bar{2}11$ topographs were studied to separate contributions of dislocations with screw and edge character. The dominant wavelengths in the 0008 and $02\bar{2}11$ topographs were 1.284 Å and 0.876 Å, respectively. With the used measurement geometry, a sample tilt angle between $\approx$5° and 20° allows recording of the symmetric topograph, without it being back reflected into the hole in the film nor past the film. The smallest practical tilt angle 7.5° was chosen to minimize image distortion created upon projection of the diffracted beam onto the x-ray film.

The back reflection measurement geometry is illustrated in Figure 1, where the incident (blue) beam is diffracted backwards (green beams) by several sets of lattice planes. Each diffracted beam will form a topograph image on the film containing information on the defect structure in the irradiated volume. In digitized topograph images, high diffracted intensity (maximum fulfillment of diffraction condition) is represented by dark and diffracted low intensity (minimum fulfillment of diffraction condition) by white colour. The beam size was 2×1 mm^2, except in the DSE measurement comparison, where a 4×3 mm^2 beam was used to save time in mapping of a large area. Diffraction spots were indexed using the software Laue Pt 3.0.[21]

Simulations of threading screw dislocations in 0008 topographs were carried out on a regular personal computer using Matlab™ as the programming interface. Images were simulated utilizing the experimental measurement conditions, i.e., 7.5° sample tilt and 80 mm distance between sample and film. All following topography images, experimental and simulated, correspond to 7.5° sample tilt and 80 mm distance between sample and film. Matlab was also used in plotting grayscale images of the simulated dislocation contrast.

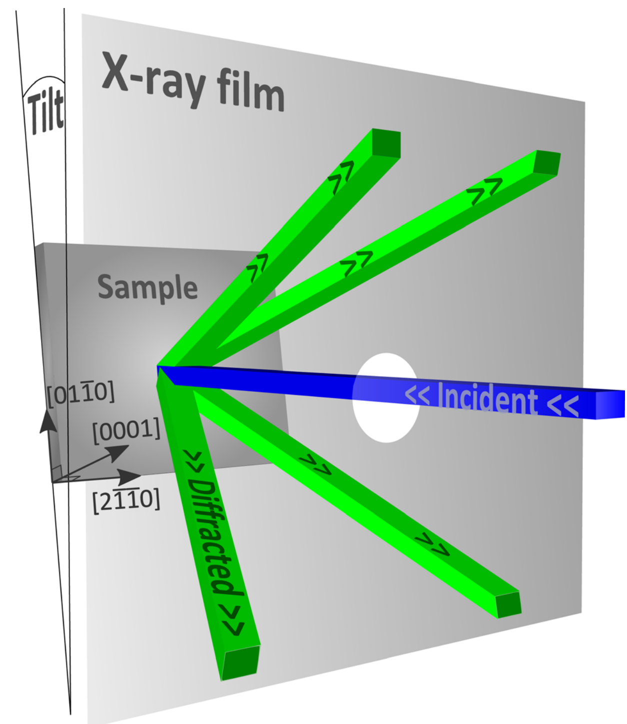

FIG. 1. Schematic representation of the back reflection topography measurement. The continuous wavelength x-ray beam (blue) traverses the hole in the film and is simultaneously diffracted back (green) onto the film by several sets of lattice planes. The incident beam and the film are perpendicular, while the sample is tilted away from the plane of the film.

Defect selective etching was employed using a KOH-NaOH eutectic alloy as the etchant. The etching temperature was 450 °C. Two etch times were used to enable inspection of etch pits before pit merging (shorter etch time, 30 min), and to provide large pits for easier low magnification visualization (longer etch time, 40 min). Details on similar DSE experiments on GaN can be found in Refs. 22 and 23. The etched sample was imaged with a differential interference optical microscope and a scanning electron microscope (SEM) operating at 5 kV acceleration voltage.

III. THEORY AND IMAGE SIMULATION

SR-XRT contrast of threading screw dislocations was simulated using the ray tracing approach, proven successful in simulating SR-XRT images of micropipes and screw dislocations in SiC.[24] In this kinematical approach, the displacement field of a TSD was used to calculate the local deviation of the diffracting plane normal vector from the normal vector of an undisturbed lattice. The displacement field $\mathbf{u}$ of a threading screw dislocation propagating in the $\hat{\mathbf{z}}$-direction is

$$\mathbf{u} = \frac{b}{2\pi} \arctan\left(\frac{y}{x}\right) \hat{\mathbf{z}}, \tag{1}$$

where b is the magnitude of the Burgers vector $\mathbf{b}$, x and y are the in-plane coordinates, and $\hat{\mathbf{z}}$ is the unit vector. The equation for the diffracting plane normal with displacement field influence is[25]

$$\mathbf{n} = \mathbf{n_0} - \nabla(\mathbf{n_0} \cdot \mathbf{u}), \tag{2}$$

where $\mathbf{n_0}$ is the undisturbed normal and $\mathbf{u}$ is the displacement field vector. The deviated normal vector $\mathbf{n}$ was then used to simulate the influence of a dislocation on the topograph image. The sample surface was divided into a two dimensional grid and the diffraction plane normals were calculated for each grid element. Each element was assumed to diffract with equal intensity, allowing the omission of depth effects in the simulation. The positions of x-rays diffracted by each element were then collected onto another two dimensional-matrix, representing the x-ray photographic film. The simulated images were formed by plotting the diffracted intensity on logarithmic scale to mimic the film response. The grid element sizes used in the simulations were 20 nm × 20 nm for the sample and 200 nm × 200 nm for the x-ray photographic film. The pixel resolution of the final simulated images was chosen to match that of the digitized experimental images. Due to limited computing power, not all TSD features were simulated simultaneously. TSDs were simulated as single dislocations, or in groups of two or three adjacent dislocations to account for the combined strain field of neighbouring dislocations. In simulating groups of dislocations, the displacement fields of individual dislocations were added before calculating the normal vectors.

Examples of simulated GaN topograph TSD images are shown in Figure 2. The image of a threading screw dislocation consists of a white circular area surrounded by a dark contrast ring and is in appearance very similar to screw dislocations and micropipes found in SiC,[18,19,25] albeit smaller. The larger SiC dislocation image size is caused by differences in lattice constants and Burgers vectors. The 6H-SiC lattice constant c is almost three times the lattice constant of GaN and the resulting strain field of an elemental screw dislocation is according to Eq. (1) directly proportional to Burgers vector magnitude, which for an elemental TSD is $b = c$. Super screw dislocations and hollow core micropipes are TSDs with a Burgers vector magnitude $b = nc$ a multiple of c. These are commonly found in SiC and result in an even larger topograph image.

Simulations of a single $1c$ TSD, a $4c$ TSD, and a group of TSDs are shown in Figures 2(a)–2(c), respectively. The simulation does not reveal whether a dislocation image with Burgers vector larger than $\mathbf{c}$ is caused by a super screw dislocation or closely spaced elemental dislocations. Hereafter, the term nc TSD will be used to denote an image caused by a threading screw dislocation or dislocation group with a net strain field corresponding to a Burgers vector $\mathbf{b} = n\mathbf{c}$. As can be seen from Figures 2(a) and 2(b), the white circle diameter increases with increasing Burgers vector, but the shape and general appearance does not change. The Burgers vector signs of single isolated dislocations cannot be determined and were assumed positive. The Burgers vector signs of neighbouring dislocations are however easily determined, as the image shapes change drastically with Burgers vector sign. An example of this is given in Figure 2(c), which displays a simulated image of a group of TSDs with the net Burgers vectors of each main lobe indicated. In the simulations, a positive Burgers vector indicates a right handed and a negative Burgers vector indicates a left handed screw dislocation.

The white circle diameter increases also with increasing sample to film distance. Figure 3 shows a plot of simulated white area diameter as a function of sample to film distance for Burgers vectors $\mathbf{b} \in [\mathbf{c}, 8\mathbf{c}]$ and 7.5° sample tilt. The 80 mm distance used in all experimental and simulated images in this study has been marked in Figure 3 with a vertical dashed line.

The Burgers vectors of elemental threading screw, edge and mixed dislocations are $\mathbf{b}_{screw} = [0001]$, $\mathbf{b}_{edge} = \frac{1}{3}[11\bar{2}0]$, and $\mathbf{b}_{mixed} = \frac{1}{3}[11\bar{2}3]$. According to the invisibility criteria[26]

$$\begin{array}{ll} \mathbf{g}\cdot\mathbf{b} = 0 & \text{for screw dislocations,} \\ \mathbf{g}\cdot\mathbf{b} = 0 \wedge \mathbf{g}\cdot\mathbf{b}\times\mathbf{l} = 0 & \text{for edge dislocations} \end{array} \tag{3}$$

($\mathbf{g}$ is the diffraction vector and $\mathbf{l}$ is the dislocation line vector), pure threading edge dislocations should not affect symmetric 0008 topographs but become visible in the asymmetric $02\bar{2}11$ topograph. Similarly, the edge component of threading mixed dislocations should only be visible in asymmetric $02\bar{2}11$ topographs. Threading mixed dislocations were observed to exhibit a sixfold black to white contrast in

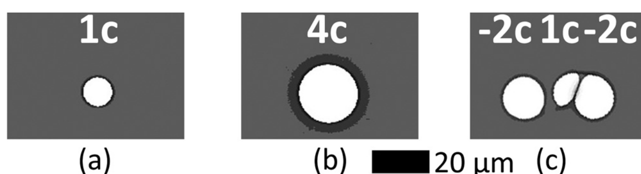

FIG. 2. Simulated images of a $1c$ TSD (a), a $4c$ TSD (b), and a group of closely spaced TSDs (c). The white area diameter increases with increasing Burgers vector.

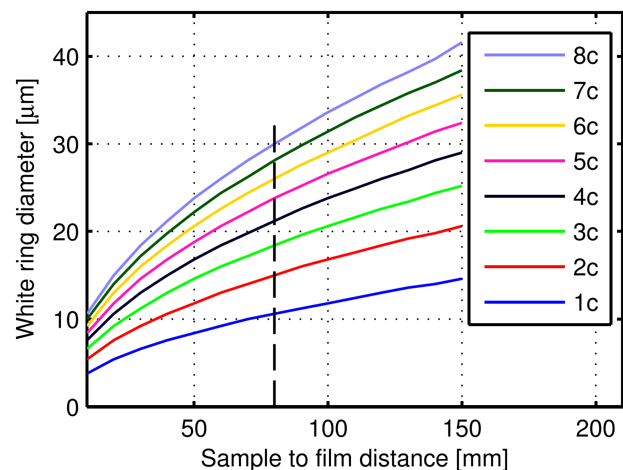

FIG. 3. Simulated white area diameters of screw dislocations with varied Burgers vectors as functions of sample to film distance. The simulations were calculated with 7.5° sample tilt. The 80 mm sample to film distance was used in all simulated and experimental images, and has been annotated with a vertical dashed line.

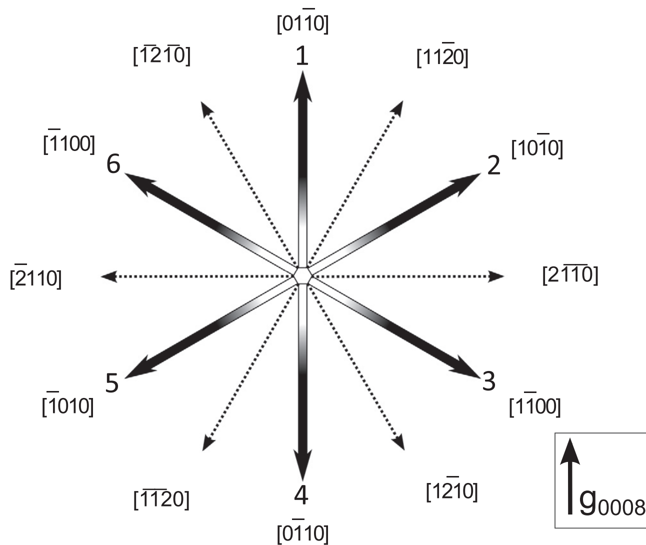

FIG. 4. Schematic representation of the six distinct black to white contrast directions of mixed dislocations observed in the back reflection topographs, the crystallographic directions and the diffraction vector $\mathbf{g}_{0008}$.

the asymmetric topographs, which the authors attribute to the edge component of the threading mixed dislocation. This is also seen in the symmetric 0008 topograph, due to the $\approx 10-12^{\circ}$ deviation of the threading mixed dislocation line vector $\mathbf{l}$ from $[0001]$ towards its Burgers vector.[27,28] Since the edge component of the mixed dislocation Burgers vector $\frac{1}{3}\langle 11\bar{2}0\rangle$ has six different orientations, the resulting inclination related contrast must also have six orientations. The six black to white contrast directions observed consistently in the recorded topographs are presented schematically in Figure 4. Additionally, the crystallographic directions and the projection of the diffraction vector $\mathbf{g}_{0008}$ are shown in Figure 4.

IV. RESULTS

A. Threading screw dislocations

Figure 5(a) displays a small area of a 0008 back reflection topograph of a bulk GaN sample as well as the projection of the diffraction vector $\mathbf{g}$. Two types of defect contrasts are observed; white circular features and smaller half moon-like features that we attribute to threading screw dislocations and threading mixed dislocations, respectively. Figure 5(b) shows a simulation of the white, screw dislocation related features with the signs and magnitudes of the Burgers vectors also indicated. The threading mixed dislocations will be addressed later in this study. The area in Figure 5 was chosen because it contains a large cluster of TSD features, thus well suited for defect studies. It should be noted that this area has a significantly higher defect density than average and is therefore not representative of the wafer scale defect structure. The upper edge of the selected area corresponds to the upper edge of the x-ray beam and is slightly uneven and blurred due to overlapping of a small continuum of images caused by lattice strain. The upper edge of the simulated image was cut identical to the experimental image edge in order to keep focus on the defect structure. As can be seen in Figure 5, the simulated TSD images are in excellent agreement with the measurement and the sizes of the simulated individual screw dislocation images match within a few pixels the sizes of the white circles in the measured topograph.

The large size clusters were simulated assuming screw dislocations with Burgers vector magnitudes $|\mathbf{b}| \in [c, 3c]$. However, as stated earlier, it is not possible to determine if an image corresponding to a screw dislocation with Burgers vector magnitude several times, the lattice constant c is truly a super screw dislocation or the result of superpositioned strain fields of several elemental screw dislocations. The area surrounding the screw dislocation core is severely distorted and scatters x-rays away from the film. The topography screw dislocation image is therefore formed by the strain field far away from the dislocation core and the simulation does not take into account whether the core is open or closed. In this work, an open core denotes a hollow dislocation core common to micropipes, and a closed core the lack of such a void. Figure 6 shows an example of this phenomenon, where an experimental image of a circularly symmetric white spot feature corresponding to a screw dislocation with Burgers vector magnitude $6c$ in Figure 6(a) has been simulated as a single screw dislocation in Figure 6(b), and as five elemental dislocations positioned in a regular pentagon with a sixth dislocation in the middle. The pentagon radius

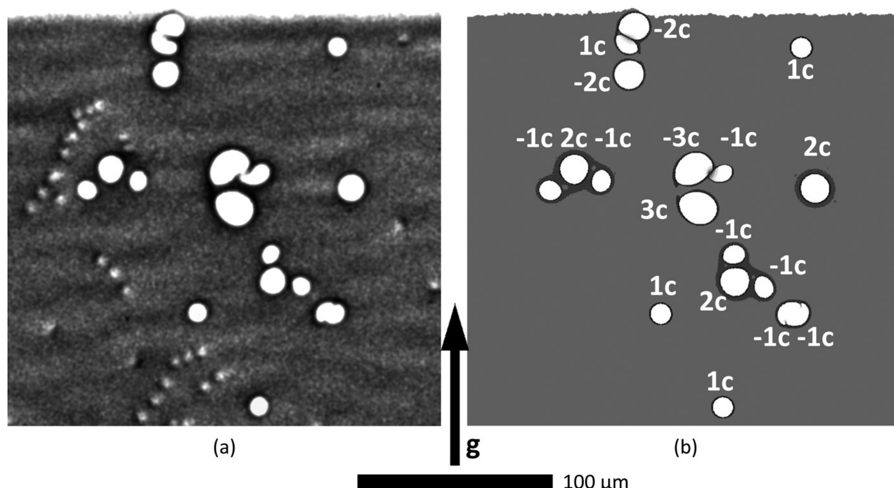

FIG. 5. 0008 back reflection (a) and simulated (b) images of individual screw dislocations and screw dislocation clusters. The signs and magnitudes of the Burgers vectors are marked on the simulated image.

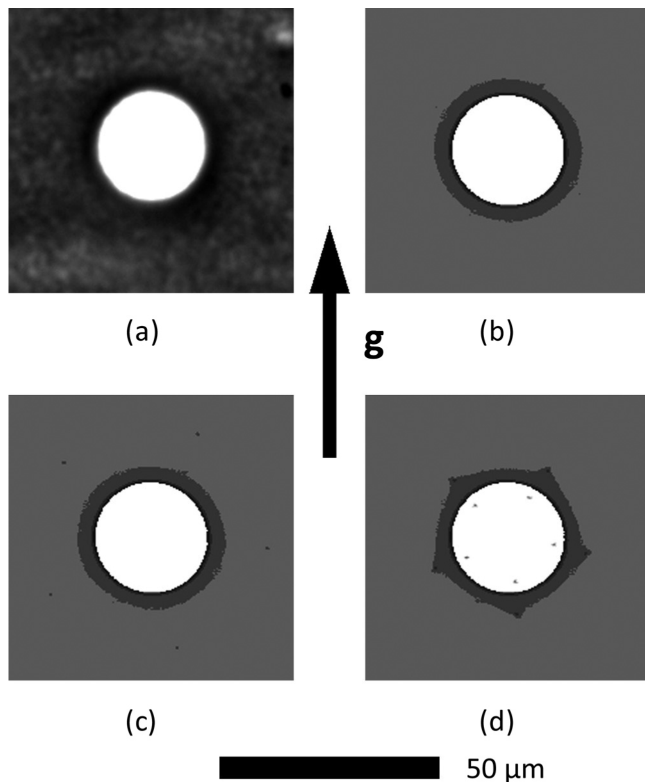

FIG. 6. Experimental (a) and simulated (b)–(d) images of a defect with white area diameter corresponding to a $6c$ net Burgers vector. (b) was simulated assuming a $6c$ dislocation, (c) and (d) assuming six separate $1c$ dislocations arranged as a single dislocation surrounded by five dislocations in regular pentagons with 2 μm and 3 μm radii, respectively. The circular symmetry fails in (d), indicating the threshold distance when the bundle is distinguished from an individual dislocation.

was 2 μm and 3 μm in Figures 6(c) and 6(d), respectively. It is clearly seen that the simulated image of a single $6c$ screw dislocation is practically identical to that of six elemental screw dislocations located within a 2 μm pentagon radius. However, the symmetry of the dark contrast ring starts to deteriorate when the radius is increased to 3 μm, as seen in Figure 6(d) and this may be regarded as the threshold distance when a bundle of six elemental screw dislocations is identified. A close look at the experimental image reveals a slight asymmetry in the dark contrast, but the asymmetry is not clear enough to be reliably attributed to TSD separation.

B. Threading mixed dislocations

Figure 7 shows symmetric 0008 (a) and asymmetric $02\bar{2}11$ (b) back reflection topographs of an area with TMDs displaying distinct black and white half moon-like contrast. The black to white contrast direction has clear sixfold symmetry as depicted schematically in Figure 4. The small area in Figure 7 was selected to clearly illustrate the six discrete contrast directions. Examples of each contrast type in Figure 7 have been labelled with numbers from 1 to 6, corresponding to the contrast directions in Figure 4. Enlargements of each contrast type for both reflections are shown in the bottom of Figure 7. Within measurement resolution, only six contrast orientations were found, even on a much greater area of several square millimetres, not shown here.

It is interesting to note that the contrast of dislocation types 2, 3, 5, and 6 are almost diffraction vector invariant, whereas the contrasts of dislocation types 1 and 4 are greatly influenced by the diffraction vector. The black and white contrast of type 1 dislocations changes to monotone dark contrast with a change in diffraction vector from $\mathbf{g} = [0008]$ to $\mathbf{g} = [02\bar{2}11]$. Type 4 dislocations display opposite behaviour with a black and white contrast change to monotone white. Type 1 and type 4 dislocations have opposite black to white contrast direction in the 0008 topograph and based on earlier discussion therefore opposite sign edge components. This results in the contrast seen in the $02\bar{2}11$ topograph, where effectively type 1 dislocations act as concave and type 4 dislocations as convex mirrors. The sizes of these dislocation images are in agreement with this conclusion, i.e., type 1 image size is the smallest and type 4 is the largest. This contrast change was observed without exceptions on a larger scale as well.

The contrast differences between the 0008 topograph and the $02\bar{2}11$ topograph in the enlargements, in Figure 7, can be further differentiated. Figure 7 shows that the type 6 contrast displays practically no contrast change between the

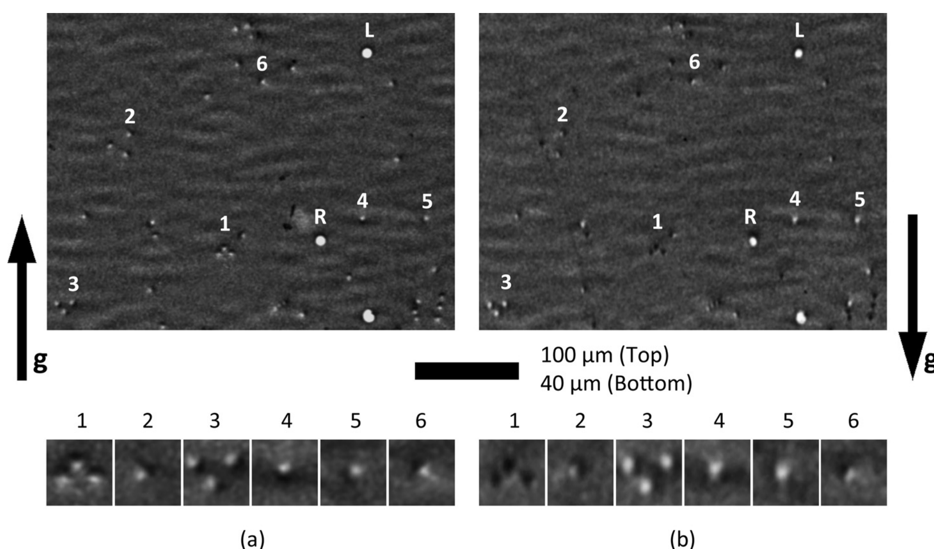

FIG. 7. Symmetric 0008 (a) and asymmetric $02\bar{2}11$ (b) topographs of mixed dislocations. Examples of six distinct black to white contrast directions are labelled with numbers 1 to 6, and enlargements of each example are shown in the bottom of the image. Two elemental screw dislocations marked L and R have opposite slant in the $02\bar{2}11$ topograph due to opposite handedness.

TABLE I. The dot products $\mathbf{b}_i \cdot \mathbf{g}$ of the diffraction vector $\mathbf{g} = [02\bar{2}11]$ and the six possible Burgers vector edge components, and the corresponding qualitative descriptions of the contrast changes.

Edge component b_i	$\mathbf{b}_i \cdot \mathbf{g}$	Observed contrast change
$\mathbf{b}_1 = \frac{1}{3}[\bar{1}2\bar{1}0]$	2	Large
$\mathbf{b}_2 = \frac{1}{3}[11\bar{2}0]$	2	Medium
$\mathbf{b}_3 = \frac{1}{3}[2\bar{1}\bar{1}0]$	0	Small
$\mathbf{b}_4 = \frac{1}{3}[1\bar{2}10]$	−2	Large
$\mathbf{b}_5 = \frac{1}{3}[\bar{1}\bar{1}20]$	−2	Medium
$\mathbf{b}_6 = \frac{1}{3}[\bar{2}110]$	0	None

symmetric and asymmetric topographs, whereas types 2 and 5 show medium change, and type 3 show a rather small change. This indicates the edge component of type 6 Burgers vector has practically no impact on the asymmetric topograph, while the Burgers vector edge components of the other types have an observable effect of varying degree. The application of the invisibility criteria, Eq. (3) on the edge component of type 6 Burgers vector should equal zero for minimum contrast change to occur. The dot products of the asymmetric $\mathbf{g} = [02\bar{2}11]$ and the six possible Burgers vector edge components $\mathbf{b}_i = \frac{1}{3}\langle 11\bar{2}0\rangle$ are presented in Table I, with qualitative descriptions of the observed contrast change. The Burgers vectors in Table I are ordered according to clockwise rotation in such a way that the dot product minimum is chosen to coincide with contrast type 6. Table I shows the contrast type 6 is likely to correspond to $\mathbf{b}_6 = \pm\frac{1}{3}[\bar{2}110]$, and that the other dot products are in reasonable agreement with the observed contrast changes. This indicates that the contrast directions of the threading mixed dislocations are indeed related to the different types of edge components, as discussed earlier.

Figure 7 displays additionally two elemental screw dislocations, marked as L and R for left and right handednesses, respectively. The screw dislocation images are highly symmetric and practically identical in the 0008 topograph, but appear elliptical with clockwise (R) and anticlockwise (L) slants in the $02\bar{2}11$ topograph. This is characteristic of threading screw dislocations and the slant direction has previously been utilized to determine handednesses of screw dislocations in SiC.[29,30]

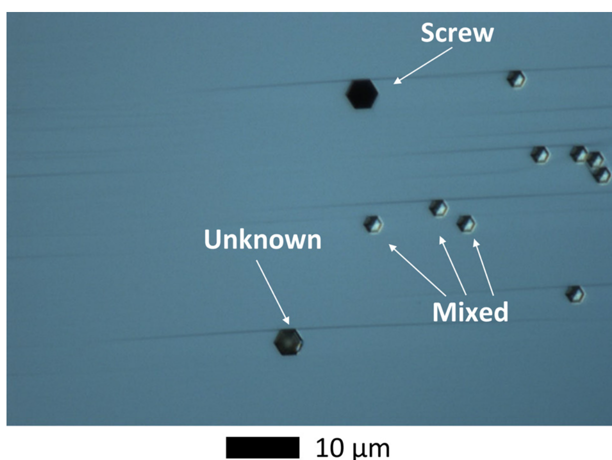

FIG. 8. DSE image showing threading screw and mixed dislocations. Dislocations with similar appearance to screw dislocations have been marked unknown and are discussed in the latter part of this study.

C. Defect selective etching

Defect selective etching was performed to investigate whether SR-XRT images corresponding to dislocations with a Burgers vector a multiple of **c** truly are single dislocations or groups of dislocations in close proximity. Before comparing DSE and SR-XRT images, the sizes and appearances of the different types of threading dislocations in DSE images needed to be determined. For this purpose, an area with all observed types of threading dislocations visible was located. An exceptionally defected area with etch pits from threading screw to mixed dislocations is presented in Figure 8. The different dislocation types are indicated by arrows and were identified based on etch pit size: the largest etch pit corresponds to the screw dislocation and smallest size pit to the mixed dislocation.[23,31,32] Additional intermediate size etch pits labelled unknown with similar appearance to screw dislocation etch pits were also identified in Figure 8. The authors believe the altered appearance of these defects is due to impurity incorporation and the matter is addressed later in this study. No threading edge dislocations were observed, although the etching conditions (450 °C eutectic KOH-NaOH, 30 min) should reveal all types of threading dislocations.[22,33]

In order to identify and study the same area with both DSE and SR-XRT, a large area (≈cm^2) was mapped with SR-XRT prior to etching the sample. The beam size used in the SR-XRT mapping was increased to $4 \times 3\,\mathrm{mm}^2$ to reduce measurement and processing time. The larger beam size however increases the fluorescence (background signal), resulting in loss of resolution. The SR-XRT pictures used in DSE comparison are therefore not as sharp as images shown earlier, but are nevertheless of acceptable quality. The following comparisons of DSE images and topographs were all conducted using the symmetric (0008) reflection.

Figure 9 illustrates a comparison between SR-XRT and DSE measurements. In the topograph, the white area in Figure 9(a) marked with the letter A corresponds to an image formed by the strain field of a 2**c** screw dislocation and the other two smaller white circles (marked B and C) to strain fields of 1**c** screw dislocations. As can be seen from the DSE

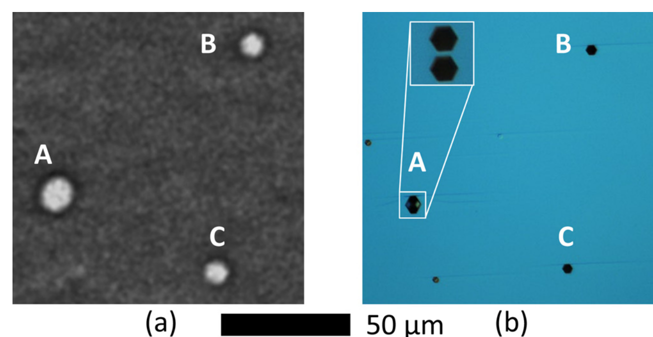

FIG. 9. Comparison of a 0008 topograph (a) and a DSE image (b). The topograph image of a 2**c** strain field, dislocation A, corresponds to two etch pits with identical dimensions to dislocations B and C. The inset in (b) shows a magnification of the two less etched pits before merging.

image of the same area, the suspected 2**c** screw dislocation (A) is composed of two separate dislocations. This is especially evident in the inset in Figure 9(b), which shows a magnification of the area around A imaged after 10 min shorter etching time. All following DSE images correspond to 40 min of etching, and their insets to 30 min of etching. The two etch pits marked A in Figure 9(b) are measured to be approximately 3.5 μm apart just exceeding the earlier determined threshold distance ≈3 μm for identification of individual screw dislocations. The topograph image of dislocations A displays indeed an asymmetric shape. Furthermore, all the etch pits in Figure 9(b) are the same size and therefore a result of the same type of dislocation.

Two sizes of etch pits are seen in Figure 10; the larger etch pits correspond to TSDs and are marked with upper case letters, whereas the smaller etch pits correspond to TMDs and are marked with numbers. Etch pit sizes in Figure 8 were used to identify the dislocation types in Figure 10. Due to the aforementioned loss of resolution, the TMDs are not seen in the topographs as clearly and five mixed dislocations have been marked with numbers 1–5 to guide the eye. Upon careful examination of the large area topograph images (not shown here), virtually all mixed type etch pits can be resolved.

Figure 10 shows additional two white dislocation images resulting from 2**c** and 1**c** strainfields, marked D and E, respectively. Contrary to Figure 9, the 2**c** topograph image (D) does not correspond to two etch pits and instead, only a single etch pit the same size as all other 1**c** etch pits is observed. It remains unclear why a 1**c** etch pit corresponds to a topography image of a 2**c** strain field. The large topograph feature size cannot be explained by two merged etch pits, since the etch pit image is a symmetric hexagon and merged etch pits are asymmetric. It is thus possible dislocation D is a super screw dislocation with burgers vector 2**c**, especially since etch pit sizes of screw dislocations and micropipes in SiC have been reported to be similar[25] and the topograph image D in Figure 10 appears more symmetric than similar images from dislocation pairs.

Figure 11 shows that a topograph image corresponding to a 2**c** strain field is composed of a pair of TMDs in close proximity and same handedness. Two pairs of mixed dislocations have been labelled with F and G. The insets in Figure 11(b) again show the etch pits separated due to a shorter

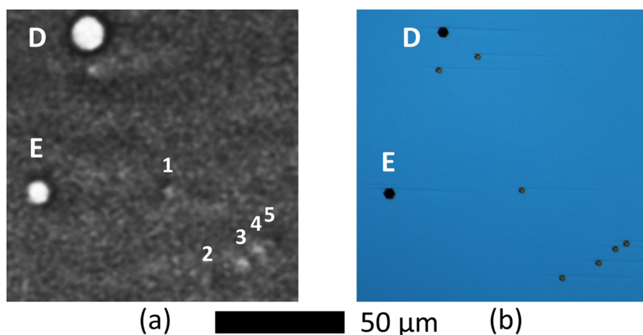

FIG. 10. Comparison of a 0008 topograph (a) and a DSE image (b). Mixed dislocations have been numbered 1–5. Dislocation D corresponds to a 2**c** strain field, but appears as a single screw dislocation etch pit.

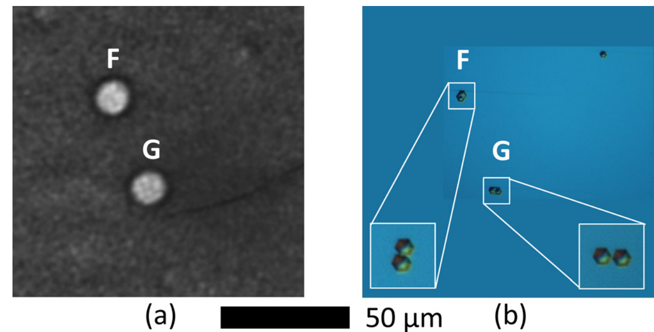

FIG. 11. Comparison of a 0008 topograph (a) and a DSE image (b). Both images of 2**c** strain fields, marked F and G, are represented by pairs of mixed dislocations in close proximity. The insets in (b) were recorded after shorter etching time and display the etch pits clearly separated.

etching time. The Burgers vectors of the TMD pair are summed and since the edge component does not affect symmetric reflections, the net Burgers vector is 2**c**.

Previous images show the DSE and SR-XRT measurements are in excellent agreement. There is virtually a one to one correspondence between dislocation images observed by SR-XRT and DSE measurements throughout the studied common area of 1.0 mm × 0.75 mm. Threading edge dislocations were not observed in the topograph images nor in the DSE images. This suggests the threading edge dislocation density is negligible, at least in the studied areas 2 mm^2 and 0.75 mm^2 of topography and DSE measurements, respectively. Since the angle between the studied asymmetric $(02\bar{2}11)$ and symmetric (0008) planes is only 18.9°, TEDs are expected to show weak topograph contrast and may fail to be observed. Edge dislocations, if present, should however be observed in the DSE images and the conclusion of very low TED density is justified. The densities of threading mixed dislocations and threading screw dislocations were determined from a large area and were $3.2 \times 10^4\,cm^{-2}$ and $3.1 \times 10^3\,cm^{-2}$, respectively. A more detailed large area analysis will be published separately.

Generally, all super screw-like topograph images are reduced to pairs or groups of adjacent dislocations, except in Figure 10. The studied DSE and SR-XRT common area included 17 topograph images of elemental screw dislocations. These match extremely well with the DSE measurements; 16 of these are matched with screw dislocation etch pits and one with a mixed dislocation etch pit. The reason for this discrepancy is still unknown.

The other discrepancy between DSE and SR-XRT is four instances where a mixed dislocation in the topograph, which appears as a screw dislocation in the DSE image. This dislocation type was earlier labelled unknown in Figure 8. An example is shown in Figure 12(b), where two pits appear to originate from screw dislocations, but dislocation H corresponds to a mixed dislocation in the topograph. Close scrutiny of the magnification insets in Figure 12(b) reveals minute differences between the two etch pit images. Etch pit H is slightly smaller and has a lighter colour, whereas etch pit I is the same size as all other "normal" screw dislocations and has a black appearance. This indicates a greater etch depth of the regular screw dislocation and a physical

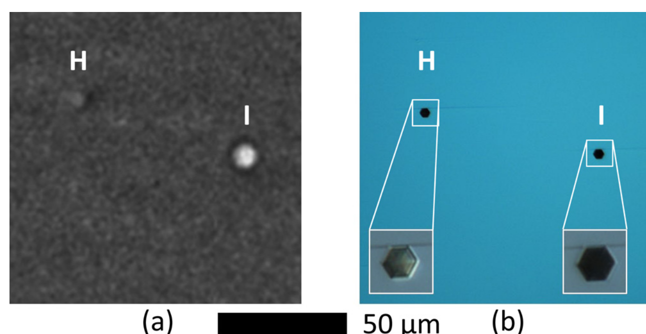

FIG. 12. Comparison of a 0008 topograph (a) and a DSE image (b). The topograph indicates H is a mixed dislocation and I is a 1**c** screw dislocation. The magnification insets in (b) reveal that seemingly similar etch pits of dislocations H and I have different appearances.

difference between the two dislocations. All four similar cases of type H demonstrate equal deviation in the etch pit appearance, in support of this conclusion. Since the corresponding topograph image of the deviant etch pit is very similar to a mixed dislocation image, the actual dislocation is also likely to be of mixed type. If the dislocation is assumed to be of mixed type enhanced etching of the mixed dislocation due to impurity incorporation is a possible explanation to the larger mixed dislocation etch pit size and to the shallower etch depth than the typical screw dislocation.

Although this conclusion is still speculative, tentative micro-Raman spectroscopy results suggest that impurities are indeed responsible for the differing appearances and the results will be published separately.[34] The unknown dislocation type was also studied by SEM to observe the shape of the etch pit side walls and etch pit bottoms. SEM images of a type H and a type I dislocation as well as a regular mixed dislocation are presented in Figure 13. The side walls of dislocation H appear differently inclined to dislocation I also in the SEM image. This is consistent with previous reports on etch pit side wall inclination difference between screw and mixed dislocations,[22,23] although reports differ on the detailed cross sectional etch pit shape.[32,35] These observations support the conclusion that dislocation H is a mixed dislocation with larger etch pit size due to faster etching, but a more detailed study is needed to confirm or reject this hypothesis.

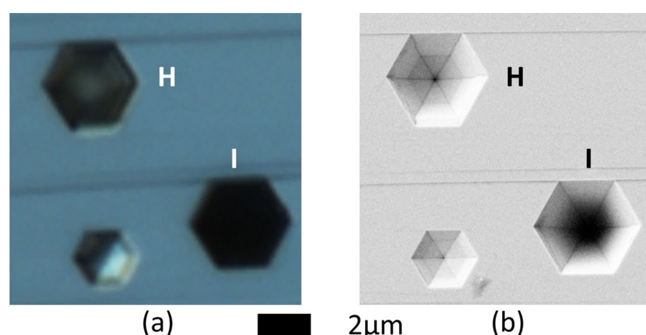

FIG. 13. Comparison of a DSE image (a) and a SEM image (b) showing a screw and a mixed dislocation as well as an additional dislocation with intermediate size. The SEM image indicates that the unknown dislocation H is also a mixed dislocation etched faster than normal.

V. CONCLUSIONS

Threading dislocations were analysed using synchrotron radiation x-ray topography. The back reflection topography images related to threading screw dislocation strain fields were simulated using a geometrical diffraction model previously utilized in SiC threading screw dislocation analysis. Simulated and experimental images of ammonothermal bulk GaN agreed very well. Two types of dislocation contrasts were observed; the screw dislocation image consists of a symmetric white circle with a dark perimeter, whereas the mixed dislocation has an asymmetric half moon-like black to white contrast with six distinct contrast orientations.

Defect selective etching measurements support these results and a comparison of SR-XRT and DSE measurements revealed that suspected superscrew dislocations are in fact closely spaced elemental screw dislocations. A practically one to one correlation was found between the two techniques and the absence of threading edge dislocations in the studied area suggests the TED density in ammonothermal GaN is extremely low. SR-XRT is therefore well suited method for non-destructive and rapid large area analysis of threading dislocations in high quality GaN crystals.

ACKNOWLEDGMENTS

We acknowledge the Synchrotron Light Source ANKA for provision of instruments at the TopoTomo beamline and we would like to thank T. Müller and H. Schade for excellent assistance. Peder Bergman, Aidan Cowley, and Patrick McNally are acknowledged for their kind assistance in topography measurements. Sintonen wishes to thank the Graduate School in Electronics, Telecommunications, and Automation (GETA), Svenska Kulturfonden and Magnus Ehrnrooth foundation for financial support. This work was also supported by the Aalto MIDE Projects DEGRADE, Aalto AEF Project MOPPI, ANKA EU Project A2013-021-002621, and the Academy of Finland Projects 13138115 and 13251864.

[1]V. Avrutin, D. J. Silversmith, Y. Mori, F. Kawamura, Y. Kitaoka, and H. Morkoc, “Growth of bulk GaN and AlN: Progress and challenges,” Proc. IEEE **98**, 1302–1315 (2010).
[2]R. Dwiliński, R. Doradziński, J. Garczyński, L. Sierzputowski, A. Puchalski, Y. Kanbara, K. Yagi, H. Minakuchi, and H. Hayashi, “Excellent crystallinity of truly bulk ammonothermal GaN,” J. Cryst. Growth **310**, 3911–3916 (2008).
[3]T. Hashimoto, F. Wua, J. S. Speck, and S. Nakamura, “Ammonothermal growth of bulk GaN,” J. Cryst. Growth **310**, 3907–3910 (2008).
[4]S. Pimputkar, S. Kawabata, J. S. Speck, and S. Nakamura, “Surface morphology study of basic ammonothermal GaN grown on non-polar GaN seed crystals of varying surface orientations from m-plane to a-plane,” J. Cryst. Growth **368**, 67–71 (2013).
[5]D. Tomida, Y. Kagamitani, Q. Bao, K. Hazu, H. Sawayama, S. Chichibu, C. Yokoyama, T. Fukuda, and T. Ishiguro, “Enhanced growth rate for ammonothermal gallium nitride crystal growth using ammonium iodide mineralizer,” J. Cryst. Growth **353**, 59–62 (2012).
[6]R. Doradziński, R. Dwiliński, J. Garczyński, L. Sierzputowski, and Y. Kanbara, “Ammonothermal growth of GaN under ammono-basic conditions,” in *Technology of Gallium Nitride Crystal Growth*, edited by D. Ehrentraut, E. Meißner, and M. Boćkowski (Springer, 2010), pp. 137–160.
[7]T. Tuomi, K. Naukkarinen, and P. Rabe, “Use of synchrotron radiation in x-ray diffraction topography,” Phys. Status Solidi A **25**, 93–106 (1974).
[8]B. Raghothamachar, M. Dudley, and G. Dhanara, *Handbook of Crystals: X-ray Topography Techniques for Defect Characterization of Crystals* (Springer, Berlin, 2010), pp. 1425–1451.

[9]T. O. Tuomi, "Synchrotron X-ray topography of electronic materials," J. Synchrotron. Rad. **9**, 174–178 (2002).
[10]M. Moore, "White-beam X-ray topography," Crystallogr. Rev. **18**, 207–235 (2012).
[11]X. Xu, R. Vaudo, C. Loria, A. Salant, G. Brandes, and J. Chaudhuri, "Growth and characterization of low defect GaN by hydride vapor phase epitaxy," J. Cryst. Growth **246**, 223–229 (2002).
[12]B. Raghothamachar, W. M. Vetter, M. Dudley, R. Dalmau, R. Schlesser, Z. Sitar, E. Michaels, and J. W. Kolis, "Synchrotron white beam topography characterization of physical vapor transport grown AlN and ammonothermal GaN," J. Cryst. Growth **246**, 271–280 (2002).
[13]J. Chaudhuri, C. Ignatiev, S. Stepanov, D. Tsvetkov, A. Cherenkov, V. Dmitriev, and Z. Rek, "High quality GaN layers grown by hydride vapor phase epitaxy: A high resolution X-ray diffractometry and synchrotron X-ray topography study," Mater. Sci. Eng., B **78**, 22–27 (2000).
[14]M. Lefeld-Sosnowska and I. Frymark, "Extended defects in GaN single crystals," J. Phys. D: Appl. Phys. **34**, A148 (2001).
[15]F. Tuomisto, J.-M. Mäki, and M. Zając, "Vacancy defects in bulk ammonothermal GaN crystals," J. Cryst. Growth **312**, 2620–2623 (2010).
[16]D. Gogova, P. P. Petrov, M. Buegler, M. R. Wagner, C. Nenstiel, G. Callsen, M. Schmidbauer, R. Kucharski, M. Zajac, R. Dwilinski, M. R. Phillips, A. Hoffmann, and R. Fornari, "Structural and optical investigation of non-polar (1-100) GaN grown by the ammonothermal method," J. Appl. Phys. **113**, 203513 (2013).
[17]S. Sintonen, M. Ali, S. Suihkonen, P. Kostamo, O. Svensk, M. Sopanen, H. Lipsanen, C. Paulmann, T. O. Tuomi, and M. Zajac, "Synchrotron radiation X-ray topography and X-ray diffraction of homoepitaxial GaN grown on ammonothermal GaN," Phys. Status Solidi C **9**, 1630–1632 (2012).
[18]X. R. Huang, M. Dudley, W. M. Vetter, W. Huang, W. Si, and C. H. Carter, Jr., "Superscrew dislocation contrast on synchrotron white-beam topographs: An accurate description of the direct dislocation image," J. Appl. Cryst. **32**, 516–524 (1999).
[19]X. R. Huang, M. Dudley, W. M. Vetter, W. Huang, S. Wang, and C. H. Carter, Jr., "Direct evidence of micropipe-related pure superscrew dislocations in SiC," Appl. Phys. Lett. **74**, 353–355 (1999).
[20]A. Danilewsky, R. Simon, A. Fauler, M. Fiederle, and K. Benz, "White beam x-ray topography at the synchrotron light source anka, research centre karlsruhe," Nucl. Instrum. Methods Phys. Res., Sec. B **199**, 71–74 (2003).
[21]X. Huang, "LauePt, a graphical-user-interface program for simulating and analyzing white-beam x-ray diffraction Laue patterns," J. Appl. Cryst. **43**, 926–928 (2010).
[22]J. Weyher, "Characterization of wide-band-gap semiconductors (GaN, SiC) by defect-selective etching and complementary methods," Superlattices Microstruct. **40**, 279–288 (2006).
[23]J. Weyher, S. Lazar, L. Macht, Z. Liliental-Weber, R. Molnar, S. Müller, V. Sivel, G. Nowak, and I. Grzegory, "Orthodox etching of HVPE-grown GaN," J. Cryst. Growth **305**, 384–392 (2007).
[24]M. Dudley, X. Huang, and W. Vetter, "Contribution of x-ray topography and high-resolution diffraction to the study of defects in SiC," J. Phys. D: Appl. Phys. **36**, A30 (2003).
[25]Y. Chen, "Defects structures in silicon carbide bulk crystals, epilayers, and devices," Ph.D. thesis (Stony Brook University, 2008).
[26]D. K. Bowen and B. K. Tanner, *High Resolution X-Ray Diffractometry and Topography* (CRC Press, 2005).
[27]H. Morkoç, *Handbook of Nitride Semiconductor Devices* (Wiley-VCH, 2008), Vol. 1, p. 823.
[28]S. Mathis, A. Romanov, L. Chen, G. Beltz, W. Pompe, and J. Speck, "Modeling of threading dislocation reduction in growing GaN layers," J. Cryst. Growth **231**, 371–390 (2001).
[29]Y. Chen and M. Dudley, "Direct determination of dislocation sense of closed-core threading screw dislocations using synchrotron white beam x-ray topography in 4H silicon carbide," Appl. Phys. Lett. **91**, 141918 (2007).
[30]Y. Chen, G. Dhanaraj, M. Dudley, E. K. Sanchez, and M. F. MacMillan, "Sense determination of micropipes via grazing-incidence synchrotron white beam x-ray topography in 4H silicon carbide," Appl. Phys. Lett. **91**, 071917 (2007).
[31]R. Dwiliński, R. Doradziński, J. Garczyński, L. Sierzputowski, M. Zajac, and M. Rudziński, "Homoepitaxy on bulk ammonothermal GaN," J. Cryst. Growth **311**, 3058–3062 (2009).
[32]L. Lu, Z. Y. Gao, B. Shen, F. J. Xu, S. Huang, Z. L. Miao, Y. Hao, Z. J. Yang, G. Y. Zhang, X. P. Zhang, J. Xu, and D. P. Yu, "Microstructure and origin of dislocation etch pits in GaN epilayers grown by metal organic chemical vapor deposition," J. Appl. Phys. **104**, 123525 (2008).
[33]M. Rudziński, E. Jezierska, J. L. Weyher, L. Macht, P. R. Hageman, J. Borysiuk, T. C. Rödle, H. F. F. Jos, and P. K. Larsen, "Defect formation in GaN grown on vicinal 4H-SiC (0001) substrates," Phys. Status Solidi A **204**, 4230–4240 (2007).
[34]M. Rudziński *et al.*, "Defects in bulk ammonothermal GaN revealed by defect selective etching" (unpublished) .
[35]T. Hino, S. Tomiya, T. Miyajima, K. Yanashima, S. Hashimoto, and M. Ikeda, "Characterization of threading dislocations in GaN epitaxial layers," Appl. Phys. Lett. **76**, 3421 (2000).